

# Simulations of the dynamics of quantum impurity problems with matrix product states

Matteo M. Wauters,<sup>1</sup> Chia-Min Chung,<sup>2,3,4</sup> Lorenzo Maffi,<sup>1</sup> and Michele Burrello<sup>1</sup>

<sup>1</sup>*Niels Bohr International Academy and Center for Quantum Devices, Niels Bohr Institute, Copenhagen University, Universitetsparken 5, 2100 Copenhagen, Denmark*

<sup>2</sup>*Department of Physics, National Sun Yat-sen University, Kaohsiung 80424, Taiwan*

<sup>3</sup>*Center for Theoretical and Computational Physics,*

*National Sun Yat-Sen University, Kaohsiung 80424, Taiwan*

<sup>4</sup>*Physics Division, National Center for Theoretical Sciences, Taipei 10617, Taiwan*

The Anderson impurity model is a paradigmatic example in the study of strongly correlated quantum systems and describes an interacting quantum dot coupled to electronic leads. In this work, we characterize the emergence of the Kondo effect by investigating the model dynamics following a quantum quench based on matrix product state simulations. The relaxation of the impurity magnetization allows for the estimate of the predicted universal scaling of the Kondo temperature as a function of the impurity-lead hybridization and quantum dot repulsion. Additionally, our simulations permit us to evaluate the current in the nonequilibrium quasi-steady state appearing after the quench. Through their values, we examine the dependence of the conductance on the voltage bias  $V_b$  and on the impurity chemical potential  $V_g$ , which displays a zero-bias Kondo peak. Our results are relevant for transport measurements in Coulomb blockaded devices, and, in particular, in quantum dots induced in nanowires.

*Introduction.* The Kondo effect is the most emblematic embodiment of strong correlations in condensed matter systems. The advances in the fabrication and measurement techniques of nanostructures allowed us to observe its distinctive zero-bias conductance peak in a wide class of systems, including gate-defined quantum dots [1, 2], nanotubes [3] and semiconducting nanowires [4].

In these mesoscopic systems, however, the dynamics of the quantum impurities at the basis of the Kondo effect is typically too fast to be observed. A complementary experimental platform has been recently offered by quantum simulators of ultracold fermionic Yb atoms [5]. In these setups, the characteristic time scales are much longer than in their solid state counterpart, thus enabling the analysis of the dynamics of the spin impurities at the basis of the Kondo effect in out-of-equilibrium transient states [6].

Inspired by these developments, in this work we analyze the dynamics of the Anderson impurity model after a quantum quench through matrix product state (MPS) simulations. By studying the transient behavior of its impurity magnetization, we provide a numerical verification of the Kondo time scale consistent with previous renormalization group results [7]. We derive the conductance of the corresponding two-terminal problem, relevant for the experimental study of Coulomb blockaded nanowires with induced quantum dots.

The out-of-equilibrium properties of quantum impurity models following quantum quenches are considered a paradigmatic playground to observe how strong correlations develop through time evolution in many-body quantum systems and have been recently studied by means of a vast set of analytical and numerical techniques [8–18]. In the following we will apply the MPS algorithm described in Ref. [19] to simulate the time evolution of the two-terminal Anderson impurity model (AIM).

*The model.* The AIM represents an electronic environment coupled with an interacting magnetic impurity; it is one of the most popular yet simple models that display the Kondo effect, and it constitutes the central element of dynamical mean field theory methods for studying correlated materials, making it a fundamental problem for many numerical algorithms [20]. Its Hamiltonian reads

$$\hat{H} = \hat{H}_{\text{leads}} + \hat{H}_{\text{tunn}} + \hat{H}_{\text{AIM}}, \quad (1)$$

where

$$\hat{H}_{\text{AIM}} = U\hat{n}_{\uparrow}\hat{n}_{\downarrow} + V_g(\hat{n}_{\uparrow} + \hat{n}_{\downarrow}), \quad (2)$$

with  $\hat{n}_{\sigma} = \hat{d}_{\sigma}^{\dagger}\hat{d}_{\sigma}$  describing the occupation of the two spin states of a single-level quantum dot, which, in turn, plays the role of the magnetic impurity and is characterized by the Hubbard repulsion  $U$  and the chemical potential  $V_g$ . Unless otherwise stated, we will focus on the particle-hole symmetric point  $V_g = -0.5U$ .

The lead Hamiltonian

$$\hat{H}_{\text{leads}} = - \sum_{\alpha,\sigma,l} t_{\alpha,\sigma,l} \left( \hat{c}_{\alpha,\sigma,l}^{\dagger} \hat{c}_{\alpha,\sigma,l} + \text{H.c.} \right) + \sum_{\alpha,\sigma,l} \mu_{\alpha,\sigma} \hat{n}_{\alpha,\sigma,l} \quad (3)$$

describes two spinful fermionic chains ( $\alpha = L, R$ ) with a spin-dependent chemical potential  $\mu_{\alpha,\sigma}$  and a hopping amplitude  $t_l = t_0 e^{-(l-1)/\xi}$  that decreases exponentially as a function of the distance from the site  $l = 1$ , with a decay length  $\xi$ . This is known as Wilson construction and it is commonly used in numerical renormalization group approaches to impurity problems. Moreover, it has been shown effective to increase both the resolution at small voltage bias, namely by mimicking an effectively larger system, and the stability of the time evolution in MPS simulation of transport problems [8, 19]. Indeed,

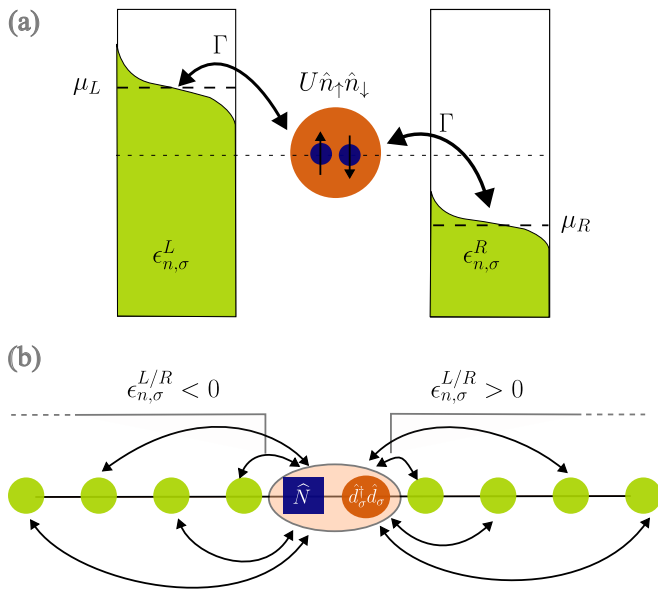


Figure 1. (a) Sketch of the AIM: a single-level quantum dot with Hubbard repulsion  $U$  is tunnel-coupled to two non-interacting leads with chemical potentials  $\mu_L$  and  $\mu_R$ . (b) Schematic representation of the MPS describing the system [19]. The sites of the chain represent single-particle orbitals and are ordered by their energy. To account for the interaction, we include an auxiliary bosonic charge site (represented by a square) which counts the number of particles inside the dot. This construction introduces long-range couplings (arrows) in the Hamiltonian MPO, which however do not constitute an obstacle for the TDVP algorithm used for the time evolution.

given the finite size  $L$ , the density of states around the Fermi energy depends on the hopping decay length  $\xi$ : the smaller  $\xi$ , the more states are shifted toward the Fermi energy, leading to a smaller energy level spacing. Therefore, a strong decay of the tunneling provides higher energy resolution to accurately determine the dynamics for states close to zero energy (thus at small bias voltages)[8].

Finally, the quantum dot and the leads are coupled with a standard tunneling Hamiltonian

$$\hat{H}_{\text{tunn}} = - \sum_{\alpha,\sigma} J_{\alpha,\sigma} \left( \hat{c}_{\alpha,\sigma,1}^\dagger \hat{d}_\sigma + \text{H.c.} \right), \quad (4)$$

where  $\hat{d}_\sigma$  destroys an electron with spin  $\sigma$  on the impurity level. Throughout this paper, we consider a uniform tunneling strength between the quantum dot and the leads  $J_{\alpha,\sigma} = J$  and we denote by  $\Gamma = 2J^2/t_0$  the effective tunneling rate in the limit of infinite bandwidth (constant density of states).

To bring the system out of equilibrium, we adopt two different quantum quench protocols [19, 21]: (i) in the *zero-bias quench*, we initialize the system with  $J = 0$  and  $\mu_L = \mu_R$ , thus preparing a product state between the impurity and the leads; at time  $t > 0$ , the leads are connected to the quantum dot ( $J > 0$ ) and the system equilibrates towards a stationary state. (ii) in the  $\mu$ -*quench*,

the system is initialized in the ground state at half filling, i.e. with uniform chemical potential  $\mu_L = \mu_R$ , and then it evolves in time after a voltage bias is turned on. The first protocol is more useful to study the relaxation of the impurity magnetization and extract the Kondo temperature, while the second leads to a fast convergence of the current to a nonequilibrium quasi-steady state. Indeed, in the  $\mu$ -quench the initial state already captures some of the non-perturbative Kondo correlations and therefore is closer to the Kondo-like quasi-steady state that arises in transport measurements.

*Matrix product state simulations.* Tensor networks offer a powerful framework to simulate the real-time evolution of quantum impurity models [8, 9, 11–13, 15, 17, 18]. To simulate the post-quench dynamics, we model the system with the MPS depicted in Fig. 1(b): each site represents a single-particle *energy* orbital of the non-interacting and decoupled system ( $U, J = 0$ ), and we compute the unitary time evolution of the closed system with the time-dependent variational principle (TDVP) [22, 23]. In particular, we expand the construction presented in Ref. [19] with the addition of the spin degrees of freedom; the MPS "sites" are ordered based on their energies [24], such that the entropy growth during the time evolution is restricted in an energy window, thus a segment of the MPS, corresponding to the voltage bias. Since the basis states (MPS "site") are ordered by their energies regardless the number of leads, introducing multiple leads (or the spin degrees of freedom) is straightforward.

The interaction  $U$  is introduced by including an auxiliary MPS site that represents the charge  $\hat{N} = \hat{n}_\uparrow + \hat{n}_\downarrow$  of the dot [19]. Tunneling events increase or decrease this charge by one. This construction is not strictly necessary for a single impurity site as in the AIM in Eq. (1), but it can easily allow for generalizations to multilevel dots with a uniform all-to-all Coulomb repulsion described by an effective charging energy.

In the chosen single-particle eigenstate basis, the dynamics is dictated only by the tunneling Hamiltonian coupling the leads with the quantum dot.  $\hat{H}_{\text{tunn}}$  is non-local in this basis, but it can be described by a matrix product operator (MPO) with limited bond dimension, such that TDVP is not hampered by the presence of these long-range interactions and can be efficiently used to simulate the dynamics for long evolution time.

The method is implemented by using ITensor library [25]. The source code can be found in Ref. [26].

*Results.* We first focus on the equilibration of the impurity after it is coupled to the *unbiased* leads (zero-bias quench). and here we set bias to zero ( $\mu_L = \mu_R$ .) The dynamics of the impurity magnetization is predicted to be characterized by two rates [27]:  $\Gamma$ , which determines the short-time and nonuniversal evolution; and the Kondo temperature  $T_K$ , whose inverse, the Kondo time  $\tau_K = T_K^{-1}$ , defines the time scale required for the formation of the Kondo screening cloud. In the renormalization group sense, the evolution for time  $\Gamma^{-1} < t < \tau_K$  is

governed by the weak-coupling fixed point of the Kondo problem [16], and  $\tau_K$  constitutes the decay time of the magnetization in this intermediate regime towards the formation of a spin singlet with the conduction electrons.

Therefore, we aim to get an estimate of the Kondo temperature as a function of the ratio between the interaction strength  $U$  and the effective tunneling rate  $\Gamma$  from the dynamics of the impurity magnetization  $\langle \sigma^z \rangle = \langle \hat{n}_\uparrow \rangle - \langle \hat{n}_\downarrow \rangle$ . We prepare the quantum dot in the polarized state  $|\hat{n}_\uparrow = 1, \hat{n}_\downarrow = 0\rangle$  and measure its evolution in time after a zero-bias quench. For this analysis, we choose  $L = 64$  as the lead length and the hopping decay length between  $\xi = 8$  and  $\xi = 32$ , depending on the energy resolution needed to accurately measure the magnetization up to times of the order of  $\tau_K$ .

We consider two values for the interaction strength,  $U = t_0$  and  $U = 0.4t_0$ , and we examine the particle-hole symmetric point  $V_g = -0.5U$ . To extract the predicted exponential dependence of the Kondo temperature from  $U/\Gamma$  [7, 12, 16], we vary the hybridization strength  $\Gamma$  between  $\sim U/20$  ( $J \sim 0.15U$ ) and  $\sim U/2$  ( $J \sim 0.5U$ ).

Figure 2(a) shows the decay in time of the magnetization for different values of  $U/\Gamma$  while we fix  $U = t_0$ . We can easily identify three regimes: at short time  $t \lesssim \Gamma^{-1}$ , the different curves collapse on each other as the relevant time scale for the relaxation of the impurity is set only by  $\Gamma$  (dashed black line). Indeed, notice that time is measured in units of  $\Gamma^{-1}$ . At longer times, the relaxation rate depends on the ratio  $U/\Gamma$ , with a slower decay the further the system lies in the strongly interacting/weak-coupling regime. For these intermediate values of  $t$ , we can extract the relaxation time by exponential fits of the data (dot-dashed gray lines). Finally, the impurity approaches a steady state with a finite magnetization; in Fig. 2(a) this last regime is visible only for  $U = 2\Gamma$ . Due to the unitary dynamics, the system keeps the memory of its initial state and a complete relaxation to a  $SU(2)$  invariant state can not be reached. Comparable results have been obtained in Ref. [12] with real-time density matrix renormalization group (DMRG) applied to a similar MPS construction.

Figure 2(b) illustrates the inverse of the relaxation times  $\tau_K(U/\Gamma)$  extracted from the magnetization decay at intermediate times [grey lines of panel (a)] as a function of  $U/\Gamma$  and for two values of the Hubbard interaction  $U$ . We interpret this quantity as the Kondo temperature  $T_K \sim \tau_K^{-1}$ . A comparison with the renormalization group prediction  $T_K \sim \sqrt{U\Gamma} e^{-\frac{\pi U}{8\Gamma}}$

$$T_K \sim \sqrt{U\Gamma} e^{-\frac{\pi U}{8\Gamma}} \quad (5)$$

(solid black line) shows excellent agreement with our data for both values of the interaction strength. In the inset the same data are displayed in logarithmic scale to emphasize the exponential dependence of the Kondo temperature from  $U/\Gamma$ . Moreover, the two datasets perfectly collapse on top of each other, highlighting the universal character of the exponential decay linked to the Kondo temperature. At very weak coupling ( $U/\Gamma \gg 1$ ) the long

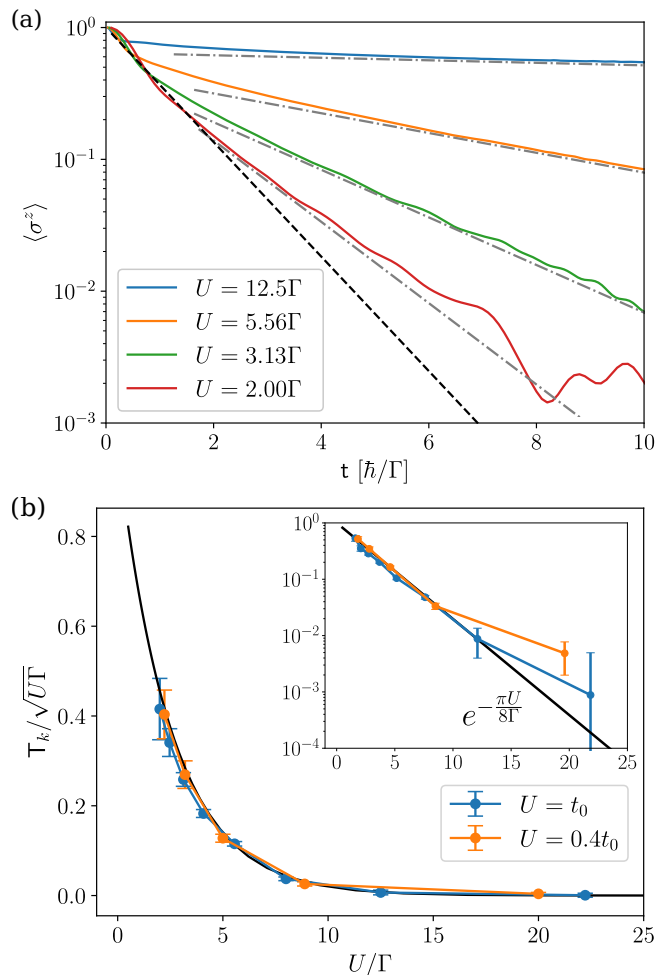


Figure 2. (a): Expectation value of the magnetization  $\langle \sigma^z \rangle = \langle \hat{n}_\uparrow \rangle - \langle \hat{n}_\downarrow \rangle$  as a function of time (in units of  $\hbar/\Gamma$ ) in a zero-bias quench. The dashed black lines indicates the short-time relaxation  $e^{-t\Gamma/\hbar}$  while the gray dot-dashed lines highlight the slow dynamics due to the Kondo resonance  $e^{-t/\tau_K}$ . The data correspond to  $U = t_0$  (b): Kondo temperature, extracted from the slow relaxation shown in panel(a), versus the effective interaction strength for two values of  $U$ . The solid black line corresponds to the RG prediction for the Kondo temperature  $T_K \sim \sqrt{U\Gamma} e^{-\frac{\pi U}{8\Gamma}}$ . The inset shows the same data in logarithmic scale to emphasize the exponential behaviour of  $T_K$ . For large values of  $U/\Gamma$  our accuracy is limited by the small signal-to-noise ratio of the time evolution of the magnetization.

evolution time needed for an accurate estimate of the relaxation time can not be reached and our data deviate from the analytical prediction. Although the entanglement growth ultimately limits our ability to simulate the evolution of large systems at long time, thus preventing the observation of Kondo correlations for very weak coupling, our method allows us to observe nonperturbative effects emerging directly from the nonequilibrium properties of the AIM.

The data in Fig. 2 are obtained with a zero-bias

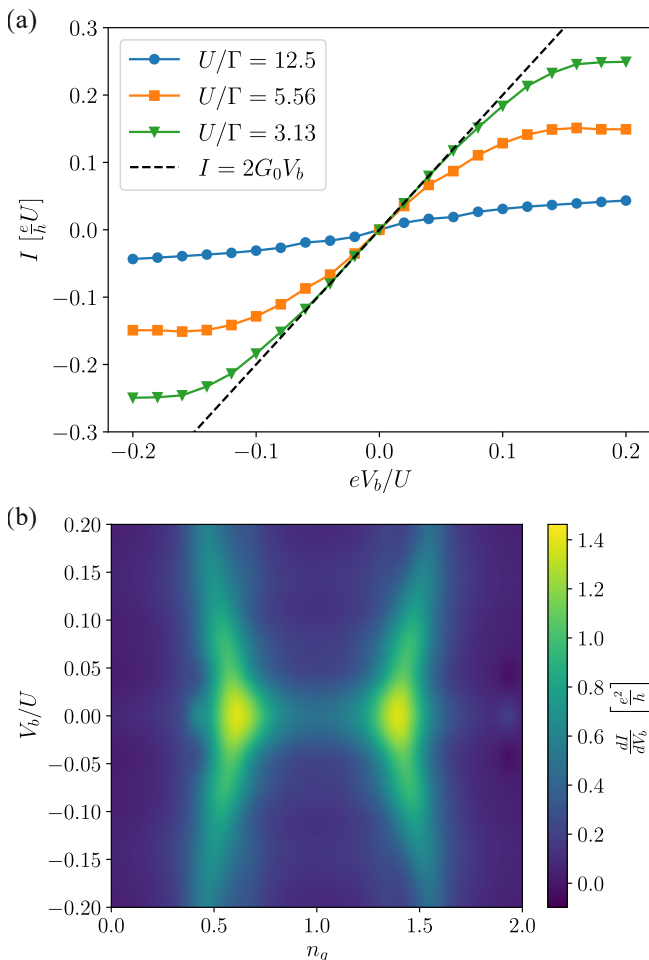


Figure 3. (a) Current vs voltage bias in the symmetric point  $V_g = -0.5U$  for three different values of the hybridization strength  $\Gamma$  and  $U = t_0$ . The dashed line corresponds to the quantized current  $I = 2\frac{e^2}{h}V_b$ . (b) Differential conductance as a function of the induced charge  $n_g$  and of the voltage bias  $V_b$  between the left and right leads, in the strongly interacting/weak-coupling regime  $U/\Gamma = 12.5$ . The zero bias peak extending between the two sequential tunneling resonances at  $n_g = 0.5$  and  $n_g = 1.5$  signals the onset of the Kondo effect.

quench, i.e., with a vanishing bias voltage. When dealing with transport properties, we evolve instead the system with a voltage bias  $V_b = \mu_L - \mu_R$  between the two leads in order to observe a quasi-stationary current. Here we use the  $\mu$ -quench protocol: in this scenario the initial state is the correlated ground state of the Hamiltonian  $\hat{H}$  (obtained through the DMRG), quenched at  $t = 0$  to a Hamiltonian with a finite voltage bias. To simulate the quench dynamics at finite bias, we also need to adjust the decay length of the hopping amplitude in the lead,  $\xi$ , such that the density of states in the leads is approximately constant in the energy interval between  $\mu_L$  and  $\mu_R$ . The convergence in the simulation parameters ( $\xi$ ,  $L$ , and the TDVP time step discretization) is reached when the cur-

rent signal displays a plateau in time long enough to reliably extract its expectation value in the quasi-steady state that develops after the quantum quench. The maximum bond dimension adopted is  $\chi = 2000$  with a truncation error  $O(10^{-8})$ .

In Fig. 3(a) we plot the quasi steady current as a function of the voltage bias for different values of the effective tunneling rate  $\Gamma$ , while keeping fixed the Hubbard interaction  $U$ , at the particle-hole symmetric point  $V_g = 0.5U$ . As we approach the strong-coupling regime  $\Gamma \sim U$ , the current tends toward a linear response with a quantized differential conductance  $\frac{dI}{dV_b} = 2\frac{e^2}{h}$ , i.e. there are two perfectly transmitting channels (dashed black line). The Kondo temperature  $T_K$  sets the extension of the bias window in which this quantization occurs [28]. In particular, as showed in Fig. 2(b), the Kondo energy scale drops down exponentially at weak coupling,  $U/\Gamma \gg 1$ , and can become smaller than the values of voltage bias we can resolve with the chosen lead length  $L = 100$  and hopping decay length  $\xi = 30$ . This explains the apparent deviation from the quantized conductance at weak coupling  $U/\Gamma = 12.5$  in Fig 3(a). Similar results are shown in Ref. [15]. We remark that, away from the strong coupling regime, we can simulate transport for voltages larger than the tunneling rate  $\Gamma$ . The main limitation comes from the fast entanglement growth when states in a large energy window contribute significantly to transport, which happens when  $V_b$  covers a significant fraction of the leads' bandwidth. In our model, this limitation becomes particularly relevant when  $V_b \sim U$ ,  $t_0$  is large enough to excite the quantum dot and there is a strong current flow due to sequential tunneling resonances at finite bias.

Fig. 3(b) illustrates the differential conductance in the weak-coupling regime ( $U/\Gamma = 12.5$ ) as a function of the bias  $V_b$  and the induced charge parameter  $n_g$  which is linked to the chemical potential as  $V_g = \frac{U}{2}(1 - 2n_g)$  and determines the expectation value of the total occupation of the quantum dot.

We derive the differential conductance in Fig. 3(b) from the simulation of a  $\mu$ -quench protocol in which the system is initialized in the ground state of  $\hat{H}$  at half filling, thus for the particle-hole symmetric point ( $n_g = 1, V_g = -0.5U$ ). At time  $t = 0$ , both the induced charge  $n_g$  and the bias voltage  $V_b$  are quenched to their final value [horizontal and vertical axis of Fig. 3(b)].

At  $n_g = 0.5$  and  $n_g = 1.5$  we observe two bright zero-bias sequential tunneling resonance, corresponding to the degeneracies between the empty and singly-occupied dot ( $n_g = 0.5$ ) or between the singly and doubly occupied dot ( $n_g = 1.5$ ). At finite voltage, the conductance peaks are prolonged along the lines  $V_b = \pm U(1 - 2n_g)$  and  $V_b = \pm U(3 - 2n_g)$ , following the resonances between each biased lead and the quantum dot. Between the two charge-degeneracy points, an extended zero bias peak indicates the onset of the Kondo effect, although for strong interaction and weak coupling we can not see the quantization of the conductance. This limitation originates mainly from the high voltage resolution needed to sam-

ple the current at energy below the Kondo temperature, which for  $U/\Gamma = 12.5$  is of the order  $T_K \sim 10^{-3}U$ , where we expect the quantized linear response. To reach such resolution in  $V_b$ , we need either a larger system size or a shorter decay length  $\xi$ . The former makes the simulations computationally more expensive, while the latter induces nonphysical effects in simulations at higher energy, preventing the calculation of the differential conductance in a wide bias range. As common in nanostructure experiments (see, for instance, Ref. [4]), this zero-bias peak does not extend to  $n_g < 0.5$  or  $n_g > 1.5$  where the ground state of the quantum dot becomes respectively, empty, or fully occupied, thus losing the doublet degeneracy necessary for the Kondo effect.

*Conclusions.* In this work we applied the tensor network method introduced in Ref. [19] to study the Kondo effect in the Anderson impurity model. In particular, we used a MPS+TDVP approach to study the dynamics of a single-level interacting quantum dot coupled to two fermionic leads after quantum quenches of the Hamiltonian parameters.

We examined both the out-of-equilibrium evolution of the quantum dot magnetization, and the electric transport features emerging in a nonequilibrium quasi-steady state after the quench.

The magnetization dynamic allows us to obtain a good estimate of the Kondo temperature as the inverse of its relaxation time when the quantum dot is coupled to unbiased leads. Such estimate is in agreement with renormalization group results [7]. In particular, the magnetization decay displays two typical time scales: the effective coupling rate with the leads and the Kondo time scale. The appearance of these two decay regimes for short and intermediate times is reminiscent of the experimental results concerning the evolution of the spin population of impurities in 1D ultracold Yb gases [5].

Concerning the study of the conductance of the system, relevant for transport measurements in nanostructures, our simulations allow us to study its evolution when a voltage bias is applied between the two leads. By looking at the emergent quasi-steady state, we can reconstruct its Coulomb blockade properties as well as

the emergence of a Kondo peak at zero bias. The latter appears when the impurity chemical potential fixes its ground state in the degenerate singly-occupied sector and the related differential conductance approaches the quantized value  $G = 2\frac{e^2}{h}$  in the strong-coupling regime.

We can simulate the system dynamics in a broad parameter range, from a strongly interacting/weak-coupling regime to a strong-coupling one, well beyond the applicability of standard perturbative master-equation approaches. Moreover, our method is not limited by single site or small impurities but can be easily extended to multilevel quantum dots or nanowires with long-range Coulomb repulsion.

Additionally, our approach can address superconducting systems, opening the path for the study of the out-of-equilibrium dynamics of the topological Kondo effect [29–31], which arises in multiterminal impurities with p-wave superconducting coupling. This kind of system can be easily described by identifying the spin degrees of freedom of the AIM as a label for different spinless leads.

In general, our method can thus be used to investigate transport phenomena in hybrid superconducting-semiconducting multiterminal devices with strong Coulomb interactions (see, for instance, Refs. [32, 33]), without being limited to a weak-coupling regime. This offers the possibility of investigating the variety of subgap states [34] that can appear in these platforms, thus providing important details towards the realization of Majorana - Cooper pair boxes and other building blocks for quantum devices [35, 36].

*Acknowledgements.* We thank J. Paaske and V. Baran for fruitful discussions. M.W., L.M. and M.B. are supported by the Villum Foundation (Research Grant No. 25310). This project has received funding from the European Union’s Horizon 2020 research and innovation program under the Marie Skłodowska-Curie Grant Agreement No. 847523 “INTERACTIONS.” C.-M.C. acknowledges the support by the Ministry of Science and Technology (MOST) under Grant No. 111-2112-M-110-006-MY3, and by the Yushan Young Scholar Program under the Ministry of Education (MOE) in Taiwan.

- 
- [1] D. Goldhaber-Gordon, H. Shtrikman, D. Mahalu, D. Abusch-Magder, U. Meirav, and M. A. Kastner, Kondo effect in a single-electron transistor, *Nature* **391**, 156 (1998).
  - [2] S. M. Cronenwett, T. H. Oosterkamp, and L. P. Kouwenhoven, A tunable kondo effect in quantum dots, *Science* **281**, 540 (1998).
  - [3] J. Nygård, D. H. Cobden, and P. E. Lindelof, Kondo physics in carbon nanotubes, *Nature* **408**, 342 (2000).
  - [4] T. S. Jespersen, M. Aagesen, C. Sørensen, P. E. Lindelof, and J. Nygård, Kondo physics in tunable semiconductor nanowire quantum dots, *Phys. Rev. B* **74**, 233304 (2006).
  - [5] L. Riegger, N. Darkwah Oppong, M. Höfer, D. R. Fernandes, I. Bloch, and S. Fölling, Localized magnetic moments with tunable spin exchange in a gas of ultracold fermions, *Phys. Rev. Lett.* **120**, 143601 (2018).
  - [6] M. Kanász-Nagy, Y. Ashida, T. Shi, C. Moca, T. N. Ikeda, S. Fölling, J. I. Cirac, G. Zaránd, and E. A. Demler, Exploring the anisotropic kondo model in and out of equilibrium with alkaline-earth atoms, *Phys. Rev. B* **97**, 155156 (2018).
  - [7] X. Wang, C. D. Spataru, M. S. Hybertsen, and A. J. Millis, Electronic correlation in nanoscale junctions: Comparison of the gw approximation to a numerically exact solution of the single-impurity anderson model, *Phys. Rev. B* **77**, 045119 (2008).
  - [8] L. G. G. V. Dias da Silva, F. Heidrich-Meisner, A. E. Feiguin, C. A. Büsser, G. B. Martins, E. V. Anda, and

- E. Dagotto, Transport properties and Kondo correlations in nanostructures: Time-dependent DMRG method applied to quantum dots coupled to Wilson chains, *Phys. Rev. B* **78**, 195317 (2008).
- [9] F. Heidrich-Meisner, A. E. Feiguin, and E. Dagotto, Real-time simulations of nonequilibrium transport in the single-impurity Anderson model, *Phys. Rev. B* **79**, 235336 (2009).
- [10] E. Gull, D. R. Reichman, and A. J. Millis, Numerically exact long-time behavior of nonequilibrium quantum impurity models, *Phys. Rev. B* **84**, 085134 (2011).
- [11] F. Güttge, F. B. Anders, U. Schollwöck, E. Eidelstein, and A. Schiller, Hybrid NRG-DMRG approach to real-time dynamics of quantum impurity systems, *Phys. Rev. B* **87**, 115115 (2013).
- [12] Z. He and A. J. Millis, Entanglement entropy and computational complexity of the Anderson impurity model out of equilibrium: Quench dynamics, *Phys. Rev. B* **96**, 085107 (2017).
- [13] F. Schwarz, I. Weymann, J. von Delft, and A. Weichselbaum, Nonequilibrium steady-state transport in quantum impurity models: A thermofield and quantum quench approach using matrix product states, *Phys. Rev. Lett.* **121**, 137702 (2018).
- [14] R. S. Souto, R. Avriller, A. L. Yeyati, and A. Martín-Rodero, Transient dynamics in interacting nanojunctions within self-consistent perturbation theory, *New Journal of Physics* **20**, 083039 (2018).
- [15] J. Thoenniss, M. Sonner, A. Lerose, and D. A. Abanin, An efficient method for quantum impurity problems out of equilibrium (2022).
- [16] M. F. Cavalcante, R. G. Pereira, and M. C. O. Aguiar, Quench dynamics of the kondo effect: Transport across an impurity coupled to interacting wires, *Phys. Rev. B* **107**, 075110 (2023).
- [17] A. Manaparambil, A. Weichselbaum, J. von Delft, and I. Weymann, Nonequilibrium spintronic transport through kondo impurities, *Phys. Rev. B* **106**, 125413 (2022).
- [18] L. Kohn and G. E. Santoro, Quench dynamics of the Anderson impurity model at finite temperature using matrix product states: entanglement and bath dynamics, *Journal of Statistical Mechanics: Theory and Experiment* **2022**, 063102 (2022).
- [19] C.-M. Chung, M. M. Wauters, and M. Burrello, Matrix product state simulations of quantum quenches and transport in coulomb blockaded superconducting devices, *Phys. Rev. B* **106**, 094308 (2022).
- [20] H. Aoki, N. Tsuji, M. Eckstein, M. Kollar, T. Oka, and P. Werner, Nonequilibrium dynamical mean-field theory and its applications, *Rev. Mod. Phys.* **86**, 779 (2014).
- [21] C.-C. Chien, M. Di Ventra, and M. Zwolak, Landauer, Kubo, and microcanonical approaches to quantum transport and noise: A comparison and implications for cold-atom dynamics, *Phys. Rev. A* **90**, 023624 (2014).
- [22] J. Haegeman, J. I. Cirac, T. J. Osborne, I. Pižorn, H. Verschelde, and F. Verstraete, Time-dependent variational principle for quantum lattices, *Phys. Rev. Lett.* **107**, 070601 (2011).
- [23] J. Haegeman, C. Lubich, I. Oseledets, B. Vandereycken, and F. Verstraete, Unifying time evolution and optimization with matrix product states, *Phys. Rev. B* **94**, 165116 (2016).
- [24] M. M. Rams and M. Zwolak, Breaking the entanglement barrier: Tensor network simulation of quantum transport, *Phys. Rev. Lett.* **124**, 137701 (2020).
- [25] M. Fishman, S. R. White, and E. M. Stoudenmire, The ITensor Software Library for Tensor Network Calculations, *SciPost Phys. Codebases*, 4 (2022).
- [26] The source code can be found in the repository <https://github.com/chiamin/QuenchTransportTwoChains>.
- [27] F. B. Anders and A. Schiller, Real-time dynamics in quantum-impurity systems: A time-dependent numerical renormalization-group approach, *Phys. Rev. Lett.* **95**, 196801 (2005).
- [28] A. Kaminski, Yu. V. Nazarov, and L. I. Glazman, Universality of the Kondo effect in a quantum dot out of equilibrium, *Phys. Rev. B* **62**, 8154 (2000).
- [29] B. Béri and N. R. Cooper, Topological Kondo effect with Majorana fermions, *Phys. Rev. Lett.* **109**, 156803 (2012).
- [30] B. Béri, Majorana-Klein hybridization in topological superconductor junctions, *Phys. Rev. Lett.* **110**, 216803 (2013).
- [31] A. Altland and R. Egger, Multiterminal Coulomb-Majorana junction, *Phys. Rev. Lett.* **110**, 196401 (2013).
- [32] T. Kanne, D. Olsteins, M. Marnauza, A. Vekris, J. C. Estrada Saldaña, S. Loric, R. D. Schlosser, D. Ross, S. Csonka, K. Grove-Rasmussen, J. Nygård, Double nanowires for hybrid quantum devices, *Advanced Functional Materials* **32**, 2107926 (2022).
- [33] A. Vekris, J. C. Estrada Saldaña, T. Kanne, T. Hvid-Olsen, M. Marnauza, D. Olsteins, M. M. Wauters, M. Burrello, J. Nygård, and K. Grove-Rasmussen, Electronic transport in double-nanowire superconducting islands with multiple terminals, *Nano Letters* **22**, 5765 (2022), pMID: 35833741, <https://doi.org/10.1021/acs.nanolett.2c01161>.
- [34] R. S. Souto, M. M. Wauters, K. Flensberg, M. Leijnse, and M. Burrello, Multiterminal transport spectroscopy of subgap states in coulomb-blockaded superconductors, *Phys. Rev. B* **106**, 235425 (2022).
- [35] Y. Oreg and F. von Oppen, Majorana zero modes in networks of cooper-pair boxes: Topologically ordered states and topological quantum computation, *Annual Review of Condensed Matter Physics* **11**, 397 (2020).
- [36] C. W. J. Beenakker, Search for non-Abelian Majorana braiding statistics in superconductors, *SciPost Phys. Lect. Notes*, 15 (2020).